Materials Advances

ROYAL SOCIETY OF CHEMISTRY

PAPER

View Article Online
View Journal

Cite this: DOI: 10.1039/d5ma01531f

Nanostructured lignin carriers for efficient flame retardant delivery in natural rubber composites

Periklis D. Alikiotis and Tizazu H. Mekonnen *

Natural rubber (NR) is a renewable elastomer with broad industrial relevance but intrinsically poor flame resistance, a limitation that is further exacerbated in foamed structures. Conventional flame-retardant strategies typically require high filler loadings that compromise mechanical performance and processability. In this work, Kraft lignin-based nanocontainers (LNCs) were engineered as multifunctional carriers to deliver ammonium polyphosphate (APP) within an NR matrix, enabling simultaneous enhancement of flame retardancy and mechanical properties at low additive contents. LNCs were synthesized *via* interfacial crosslinking and stably incorporated into NR latex using surfactant-assisted dispersion, yielding nanocomposites with preserved particle sizes of approximately 300 nm and minimal aggregation after coagulation and drying. At a loading of 10 wt% LNC, the resulting NR composites exhibited a 35% improvement in comprehensive combustion indices, a 43% reduction in peak heat release rate, and a 57% decrease in linear burn rate relative to neat NR, while achieving a UL-94 HB rating where the control failed. Concurrently, mechanical performance was significantly improved, with a 127% increase in toughness alongside gains in strength, modulus, and elongation at break. Notably, foamed NR/LNC composites demonstrated further enhancement in flame resistance, exhibiting higher limiting oxygen index values and nearly half the linear burn rate of their solid counterparts, indicating a synergistic interaction between the intumescent nanocontainers and the porous foam architecture. Overall, lignin nanocontainer-mediated delivery of flame retardants provides an effective, bio-based strategy to balance fire safety and physicomechanical performance in natural rubber systems, outperforming conventional bulk additive approaches.

Received 30th December 2025,
Accepted 10th January 2026

DOI: 10.1039/d5ma01531f

rsc.li/materials-advances

1. Introduction

Currently, 79% of all plastic produced either reaches the environment or a landfill, degrading slowly and leeching microplastics and other toxic pollutants directly into the environment.[1] Given rising environmental concerns, the development of sustainable and renewable materials is of great importance. Natural rubber (NR) is among the few polymeric hydrocarbons that is generated directly through biological means,[2] and is used widely where it may experience high-temperature or ignition sources, such as in automotives, electrical insultation, and construction.[3,4] With a limiting oxygen index (LOI) of just 18%,[5] NR is already quite flammable, but it is also used as a foamed material which increases flammability due to the large surface area and hydrocarbon-based matrix.[6] Alternative polymeric foams are typically petroleum based and exert significant environmental stress throughout their life cycle.[7]

The mechanism of flame propagation can be summarized as the thermal decomposition of the condensed phase (the polymer) that releases volatile gases that mix with oxygen in the gas phase which combust, releasing heat, auto-accelerating this process.[8] This bestows complexity at measuring a material's capability of burning. As such, a variety of flammability tests (most notably UL-94, LOI[9]) exist that must be passed in order for a material to become approved for use in various industries.[10] Given these difficult standards, polymers are typically filled with flame retardants (FRs) at very large percentages,[3] which in some cases compromises the processability and physicomechanical properties.[11]

Halogenated FRs, known to provide excellent fire inhibition,[12] have come under scrutiny due their impact on the environment and general safety concerns,[13] which has spawned research into alternatives FR, namely bio-based ones.[14] Phosphorus-based FRs have been a popular point of research due to their multiple flame retarding pathways, versatility, and efficiency at low loadings.[14] Ammonium polyphosphate (APP) is a key contender as it includes both an acid source and a blowing agent making it an intumescent FR.[15] But when combusted in the presence of carbonaceous material, it can form a porous char layer which resists fire propagation by slowing thermal feedback.[16,17] While there exist a variety of

Department of Chemical Engineering, Institute of Polymer Research, Waterloo Institute of Nanotechnology, University of Waterloo, N2L 3G1, Waterloo, ON, Canada. E-mail: tmekonnen@uwaterloo.ca

phosphorus-based FRs, APP is typically utilized for its properties garnering Melamine polyphosphates, for example, can be processed at larger temperatures, but have much larger percentages of nitrogen compared to phosphorus, having improved foamability, but lower radical-scavenging capability in comparison.[18,19] The inclusion of lignin, the second most abundant biopolymer and a largely charring material, would only add to the charring ability of a FR.[20,21] Kraft lignin in particular is the most abundant source of lignin, as it is the most popular industrially-sourced lignin, generated as waste from the pulp and paper industry.[22,23] FR polymeric nanocomposites in particular can make tremendous improvements in a material's flame retardancy whilst improving its mechanical properties[8] in comparison to traditional mineral FR composites, which require large loadings and tend to deteriorate a polymer's mechanical properties.[3] A nano-lignin & APP FR would balance the need for a reduction in toxicity, the development of a bio-based filler, and the reduction in filled content.

This work focuses on expanding the work done by Peil *et al.*[6] by utilizing Kraft lignin to construct lignin nano-containers (LNCs) to deliver APP, a hydrophilic FR, to NR, a hydrophobic polymer. The composites are compared to a composite where lignin and APP are added in bulk form at the latex stage to compare the benefits and drawbacks of each method. Additionally, this work maintains the effort of using biological materials in biocompatible polymers, in contrast to similar works that utilize APP in epoxy resin composites[24] or lignin and APP in polyurethane.[25]

2. Experimental

2.1. Materials

Sodium hydroxide (NaOH, ≥97.0%, Sigma-Aldrich – Oakville, ON, CAS No.: 1310-73-2), purified Kraft lignin (Alberta Pacific Forest Industries Inc. – Hinton, Alberta, ON), ammonium polyphosphate (APP, Aaron Chemicals LLC – San Diego, CA, USA), toluene (Sigma-Aldrich), sorbitan monooleate (Span 80, Sigma-Aldrich, CAS No.: 1338-43-8), oleic acid (90%, Sigma-Aldrich, CAS No.: 112-80-1), polyoxyethylene sorbitan trioleate (Tween 85, Sigma-Aldrich, CAS No.: 9005-70-3), isophorone diisocyanate (IPDI, 98%, Sigma-Aldrich, CAS No.: 4098-71-9), polyethylene glycol sorbitan monolaurate (Tween 20, Sigma-Aldrich, CAS No.: 9005-64-5), natural rubber latex (61.52 wt% NR, Chemionics Corp – OH, USA), azodicarbonamide (ADC, Sigma-Aldrich, CAS No.: 123-77-3), dicumyl peroxide (DCP, Sigma-Aldrich, CAS No.: 80-43-3), ZnO (Zinc oxide, Sigma-Aldrich, CAS No.: 1314-13-2), dimethyl sulfoxide (DMSO, Sigma-Aldrich, CAS No.: 67-68-5).

2.2. Methods

2.2.1. Lignin nanocontainer (LNC) synthesis. The aqueous phase comprised of water (25 mL), NaOH (2 g), lignin (2 g), and APP (4.5 g) were added to a beaker and placed on a hotplate with magnetic stirring capability (400 rpm, 100 °C) until all components were completely dissolved. The evaporated water was replenished to maintain the composition. The organic phase comprised of toluene (95 mL), Span 80 (1 mL), oleic acid (0.75 mL), and Tween 85 (0.5 mL) were added to a large beaker and mixed thoroughly (400 rpm) at room temperature before proceeding. The crosslinking solution was comprised of toluene (23 mL), IPDI (0.43 mL), and Span 80 (0.5 mL).

Using a needle-tipped syringe (1 mm ID), the aqueous phase was added dropwise (~2 drops s^{-1}) to the organic phase under aggressive homogenization (IKA homogenizer, 10 000 rpm) until the aqueous phase was completely incorporated. The resulting emulsion was transferred to a hotplate with aggressive stirring (700 rpm). While stirring, the crosslinking solution was added dropwise (~2 drops s^{-1}) *via* burette to the emulsion, covered, and kept stirring overnight to generate the lignin nanocontainers (LNCs).

The emulsion was centrifuged (4200 rcf, 5 mins) to separate the LNC from the toluene but needed to be washed to remove the surfactants. The supernatant was discarded, and fresh toluene was added to each centrifuge tube. Then, each centrifuge tube was sonicated (1 min, 92% amplitude) to scrub each LNC of surfactant and was centrifuged again. This washing procedure was repeated until the supernatant was clear, typically 3 times total. The resulting pellet was laid out in a fume hood to allow for residual solvent to evaporate. The solvent-free pellets were freeze-dried to obtain a dried LNC powder. This procedure is summarized visually in Scheme 1.

2.2.2. NR composites fabrication. The powdered LNCs were pre-dispersed in water at a ratio of 30 mL water, 2.5 g (dry weight) LNC, and 1 mL Tween 20, and were sonicated (26mins, 92% amp). Multiple of these LNC dispersions were made to obtain larger filler contents. Calculated amounts of LNC dispersion (Table 1) was then added to NR latex under homogenization (IKA homogenizer, 10 000 rpm, 4 mins) to achieve proper dispersion. The latex/LNC mixture was transferred to a large silicon mold to form a thin layer and then dried in a vacuum oven at 500 mTorr and 50 °C to coagulate the rubber as quickly as possible to prevent agglomeration of the LNCs. The NR/LNC formulations were then mixed using a HAAKE Rheomix 3000 batch mixer (Thermo-Fisher Scientific Inc., Waltham, MA, USA) with foaming agents in proportions shown in Table 1. The sample names in Table 1 indicate the corresponding weight percentage of the FR added (*i.e.* 10-LNC is 10 wt% LNC, 10-L + A is 10 wt% of a lignin, APP, and NaOH blend that follows the same ratios as used during the LNC synthesis).

After batch mixing, samples were formed into compression molded sheets in a Carver compression mold using an 80 mm × 80 mm × 5 mm mold at 140 °C and 1000 psi for 5 mins. The compression molded sheets were allowed to cool to room temperature before being placed in a 130 mm × 130 mm × 5 mm compression mold spacer at 180 °C and 3000 psi for 3 mins to degrade the ADC and foam the specimens. At these conditions, only the samples N and 10-LNC foamed, indicating the need for a case-by-case optimization relating to foaming agent and filler concentration. All samples were tested to explore the effects of foamed *vs.* non-foamed specimens on

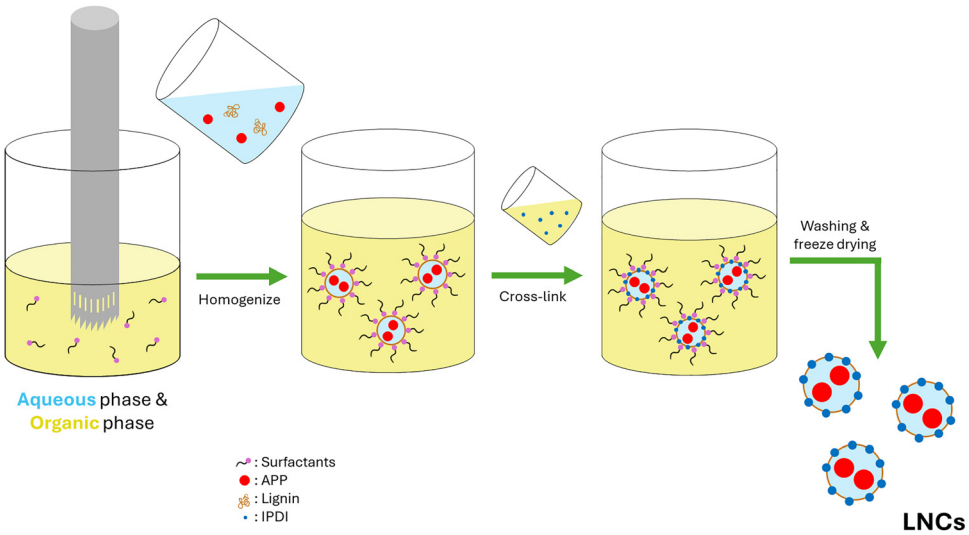

Scheme 1 Synthesis of APP-filled LNCs *via* emulsification, crosslinking, and freeze drying.

Table 1 Recipe for sample in per hundred rubber (phr)

	Control (N)	2.5-LNC	5-LNC	10-LNC	10-L + A*	15-LNC
Rubber	100	100	100	100	100	100
LNC (*or lignin, NaOH & APP)	0	2.8	5.9	12.5	12.5	19.8
ADC	10	10	10	10	10	10
DCP	1	1	1	1	1	1
ZnO	1.5	1.5	1.5	1.5	1.5	1.5

the performance of the flame retardant. Going forward, the N and 10-LNC samples that foamed will be referred to as N (f) and 10-LNC (f), respectively. The fabrication of the LNC composites is summarized in Scheme 2.

2.2.3. Fourier transform infrared (FTIR) spectroscopy. Thermo-Scientific Nicolet 6700 FTIR equipped with attenuated total reflectance (ATR) was used to investigate the change in functional groups throughout the crosslinking reaction to form the LNCs. Lignin and IPDI were mixed in DMSO, placed upon the ATR plate which was heated to 100 °C and held for 30 minutes. Spectral scans were taken every 10 minutes. The absorbance for each sample was collected over a spectral range of 500–4000 cm^{-1} measured with 64 scans at a resolution of 8 cm^{-1}.

2.2.4. Dynamic light scattering (DLS). The zeta potential and hydrodynamic radius of LNC emulsions and dispersions was measured using a Malvern Zetasizer Nano-ZS. Bulk solutions (0.5 mL) were diluted in their respective solvent (4 mL) in a glass cuvette, and three measurements were taken at 25 °C per sample.

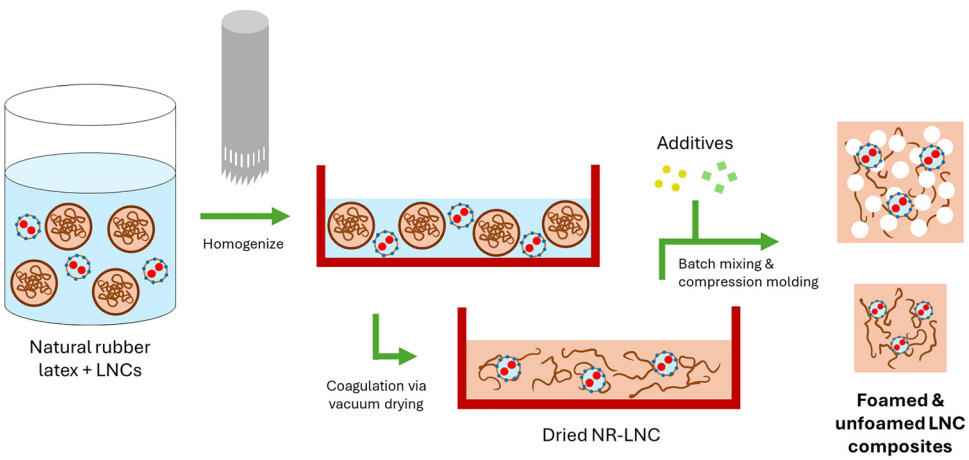

Scheme 2 Fabrication of NR-LNC composites.

2.2.5. Thermogravimetric analysis (TGA). The thermal stability of the rubber composites was evaluated using a TA Instruments Discovery TGA 55. The following method was used: 20 °C min^{-1} ramp to 105 °C, isothermal for 5 mins, 20 °C min^{-1} ramp to 650 °C. All samples were subjected to the test twice, once in an inert environment (60 mL min^{-1} nitrogen) and once in an oxidative environment (60 mL min^{-1} air), with analysis occurring on a dry basis, after the isothermal step at 105 °C.

2.2.6. Mechanical property testing

2.2.6.1. Tensile test. Tensile properties were evaluated by a Shimadzu AGS-X using a 500 N load cell. Four samples of 40 mm × 3 mm × 4 mm were tested for each formulation in a randomized order at 500 mm min^{-1}. Results for ultimate tensile strength, elastic modulus, elongation at break, and toughness were recorded.

2.2.6.2. Hardness. Each rubber composite had their hardness tested in triplicate using a Type O Durometer in accordance with ASTM 2240. Compression molded specimens with thickness of 0.5 cm were used for the test, with all measurements occurring at least 12 mm from the edge and after 10 seconds of applying the durometer.

2.2.7. Flammability testing

2.2.7.1. Combustion indices. By analyzing the TGA and derivate thermogravimetric (DTG) curves in an oxidative environment, the combustion performance of each sample can be assessed using combustion indices.[26,27] The values of comprehensive combustion index (S), flammability index (C), ignition index (D_i), and burnout index (D_b), were calculated as follows:

$$S = \frac{R_{max} \times R_{avg}}{T_i^2 \times T_b} \quad (1)$$

$$C = \frac{R_{max}}{T_i^2} \quad (2)$$

$$D_i = \frac{R_{max}}{t_i \times t_{max}} \quad (3)$$

$$D_b = \frac{R_{max}}{\Delta t_{1/2} \times t_{max} \times t_b} \quad (4)$$

where R_{max} and R_{avg} are the maximum and average mass loss rate (%/min), T_i and T_b are the ignition and burnout temperature (K), t_i, t_{max} and t_b are the ignition, maximum, and burnout times (min), respectively, and $\Delta t_{1/2}$ is the time spent at or over half the value of R_{max} (min).

The overall ability of the material to ignite and sustain combustion is represented by S, whereas C focuses on the ability of the material to ignite. D_i and D_b reflect the material's ability to reach the ignition point and maintain combustion, respectively. Larger values for all these indices indicate the increased flammability of a material, whereas lower values indicate increased flame retardancy.

2.2.7.2. Simultaneous differential thermal (SDT) analyzer. The heat release of select samples during decomposition in an oxidative environment was evaluated using a TA Instruments Q600 SDT. Rubber samples of 10–20 mg underwent the following method: 20 °C min^{-1} ramp to 105 °C, isothermal for 5 mins, 20 °C min^{-1} ramp to 650 °C under 60 mL min^{-1} of air. Heat release data was analyzed on a dry basis, after the 105 °C isothermal step which removes excess moisture. Among other combustion calorimetry parameters, including the peak heat release rate (pHRR), mean heat release rate (mHRR), temperature at the pHRR (T_{pHRR}), and the total heat release (THR), the fire growth capacity (FGC) parameter[28] was calculated as follows:

$$FGC = \left(\frac{THR}{T_{95\%} - T_{5\%}}\right)\left(\frac{T_{95\%} - 298\ K}{T_{5\%} - 298\ K}\right) \quad (5)$$

where $T_{95\%}$ and $T_{5\%}$ represent 95% and 5% conversion on the basis of heat release for each sample during the test.

2.2.7.3. UL-94 horizontal burn (HB) test. The rating of HB of the UL-94 flame tests is the lowest rating in the standard, meant for samples that readily burn at atmospheric conditions. Samples were tested in accordance with ASTM D635 and were assigned the HB rating if they achieved a horizontal burn rate ≤ 40 mm/min or stopped burning prior to reaching the 100 mm reference line.

2.2.7.4. Limiting oxygen index (LOI). The LOI for all samples was measured in accordance with ASTM D2863. Type IV specimens of dimensions 76 mm × 6.5 mm × 3 mm were cut from compression molded sheets and were tested using top surface ignition. Samples were conditioned at room temperature for a minimum of 72 h prior to testing.

3. Results and discussion

3.1. LNC characterization

3.1.1. FTIR analysis. To demonstrate the crosslinking reaction between lignin and IPDI, both compounds were mixed and the evolution of their FTIR spectra evaluated over the course of 30 minutes (Fig. 1a) alongside the spectra of the individual components and at the initial starting time (Fig. 1b). Being a diisocyanate, IPDI carries two N═C═O groups with their spectrum reading at 2255 cm^{-1} (Fig. 1b), falling within the typical range of isocyanates of 2280 to 2240.[29,30] As significant features to lignin chemical structure, vibrations ascribed to syringyl and guaiacyl at 1305 and 1018 cm^{-1}, respectively were noted, between all spectra containing lignin (Fig. 1c).[22] Due to lignin's abundance of hydroxyl groups,[22,31] the reaction between these groups and IPDI could generate urethane linkages, as has been done before with Kraft lignin,[31] with the proposed reaction scheme shown in Fig. 1.

Since lignin is a random biopolymer, its hydroxyl groups are both aromatic and aliphatic,[31] so the resulting linkages are

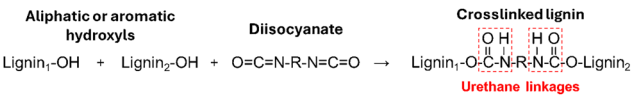

Fig. 1 Proposed crosslinking reaction scheme.

expected to be a mix of aromatic esters and aliphatic ethers, with these peaks visible at 1260 and 1136 cm^{-1} (Fig. 1d). Additionally, the formation of urethane linkages in this system form amide groups, which generate N–H (3340 to 3250) and C═O (1680 to 1630) stretching peaks,[29,30] and were found at 3326 cm^{-1} (Fig. 1d) and 1670 cm^{-1} (Fig. 1d) but only in the final reaction spectrum. The diisocyanate peak mentioned previously was visible throughout the entire reaction and indicates that some isocyanate functional groups remained unreacted or partially reacted within the lignin. Due to the generation of ester, ether, and amide groups over the course of the reaction, it was concluded that lignin was successfully crosslinked with the addition of IPDI (Fig. 2).

3.1.2. DLS. Prior to centrifugation, one batch of the LNC emulsion was stirred overnight without the addition of crosslinker added, while another batch contained the crosslinker. Afterwards, the particle size for each batch was measured to further explore the effect of the interfacial crosslinking between lignin and IPDI. The fresh emulsion exhibited a primary particle diameter of approximately 200 nm (Fig. 3a). After overnight stirring, the batch with crosslinker retained a much smaller mean particle size of roughly 100 nm (Fig. 3b), whereas the batch without crosslinker underwent significant coalescence, with its major particle size distribution shifting toward a mean of nearly 1 μm (Fig. 3c).

To ensure the proper dispersion of the LNCs in NR latex, they were dispersed in both DI water and DI water with Tween 20, and their particle size distributions were measured, as shown in Fig. 4. The solution with no surfactant (Fig. 4a) showed major agglomeration, with the bulk particle size well over 1 μm, whereas the solution with surfactant (Fig. 4a) retained the particle size to roughly 300 nm, reinforcing the importance of surfactant use when forming the NR-LNC composites. To further corroborate this conclusion, the zeta potential was measured for the Tween 20 sample. This resulted in a zeta potential of −42 mV, indicating a good stability of the particles within water, due to electrostatic repulsion when using Tween 20.

3.1.3. SEM imaging. After fabrication of the composites, EDS was performed to verify the LNCs composition (Fig. 5), while elemental mapping and SEM images were acquired to determine their dispersion (Fig. 6 and Fig. 7, respectively). As shown in Fig. 5, the area marked in red from the SEM image contained a white particle roughly 300 nm in diameter. EDS in this area determined 1.09 wt% phosphorus and 0.75 wt% sodium. Since phosphorus and sodium are major components of the LNC synthesis, originating from APP and sodium hydroxide, respectively, this confirms that the white particle is indeed an LNC. This was further supported when considering the N sample contained no white particles nor detectable phosphorus or sodium (Fig. S1). Elemental mapping (Fig. 6b) further demonstrated that the distribution of phosphorus coincided with the white particulates (Fig. 6c) observed in Fig. 6a. The apparent noise was attributed to sample thickness, as some LNCs located outside the SEM focal plane (Fig. 6a) were still detected during elemental mapping.

When comparing 10-LNC to 10-L + A, it can be observed that the LNC sample's white particulates overall remained spherically shaped and dispersed (Fig. 7a), whereas the L + A sample had webs of white stretching between gaps in the rubber's

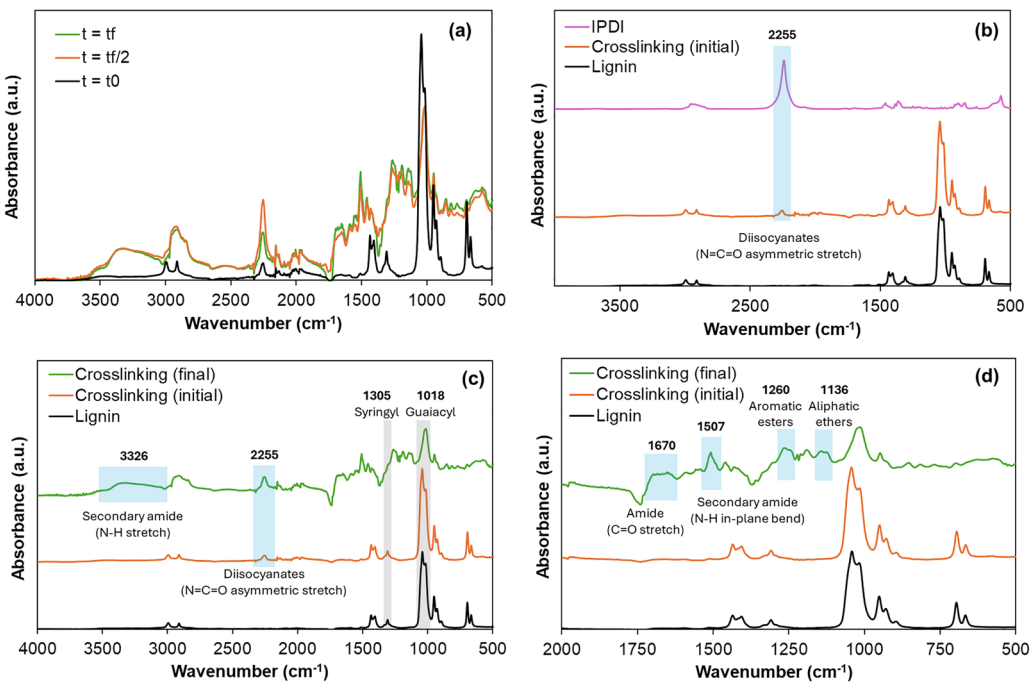

Fig. 2 ATR-FTIR spectra of the crosslinking reaction over time (a), comparing reactants with the initial reaction spectrum (b), and comparing the evolution of new peaks from the crosslinking reaction (c) and (d).

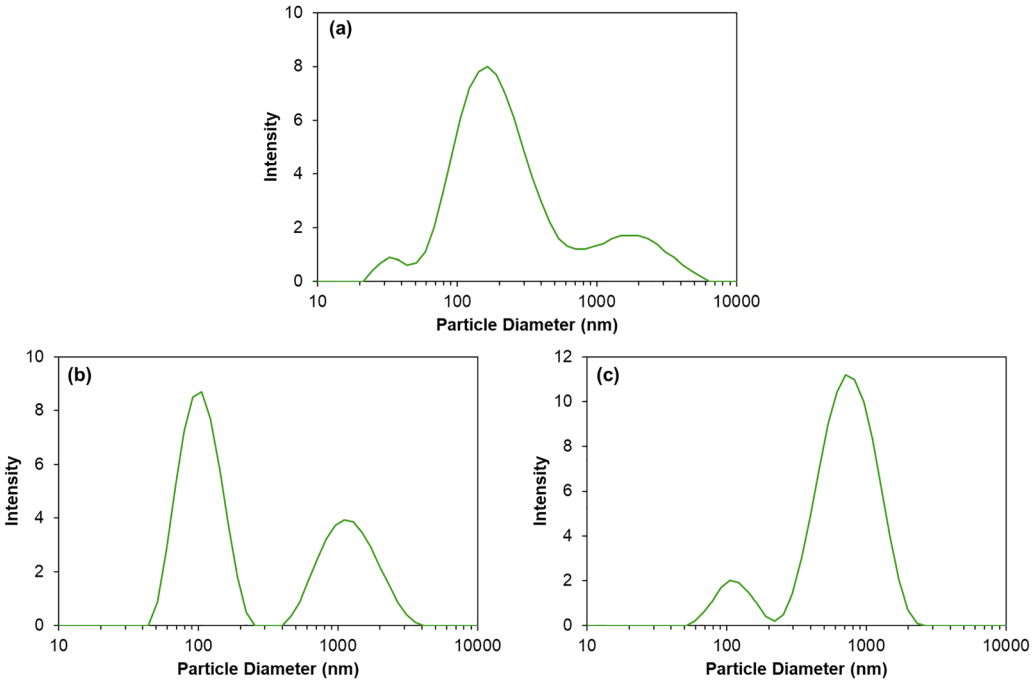

Fig. 3 DLS plots for the fresh emulsion (a), and the emulsion kept overnight either with or without crosslinking ((b) and (c), respectively).

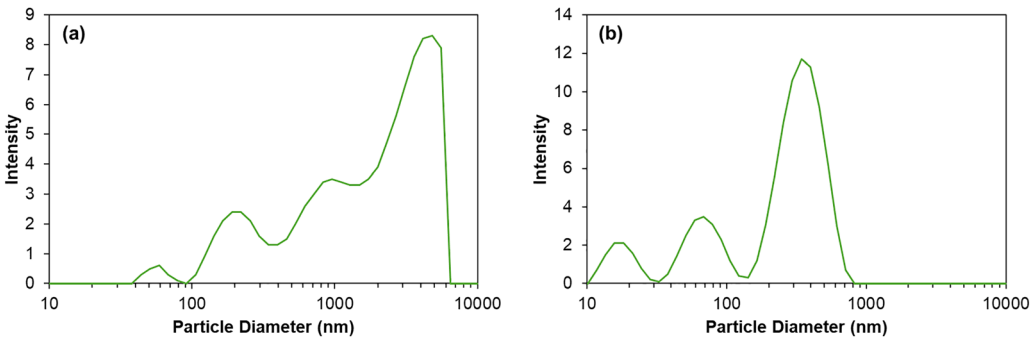

Fig. 4 DLS plots for LNCs dispersed in water (a) and water + Tween 20 (b).

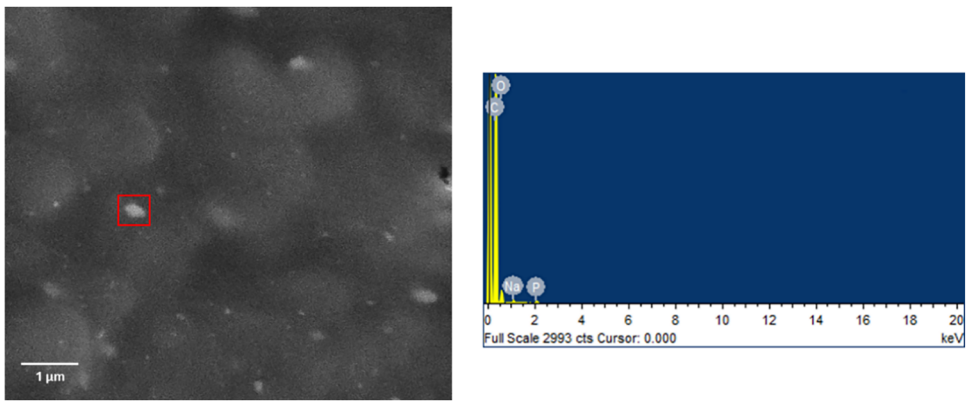

Fig. 5 EDS from area marked in red for sample 5-LNC.

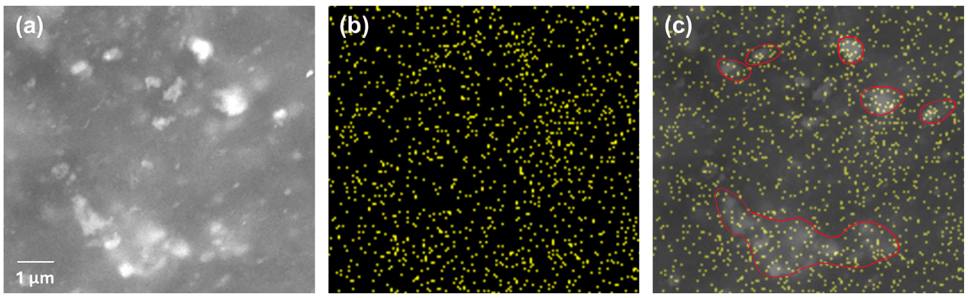

Fig. 6 E-SEM image of sample 5-LNC (a), with elemental mapping on phosphorus of the image (b), and overlaying the previous images to indicate overlaps (c).

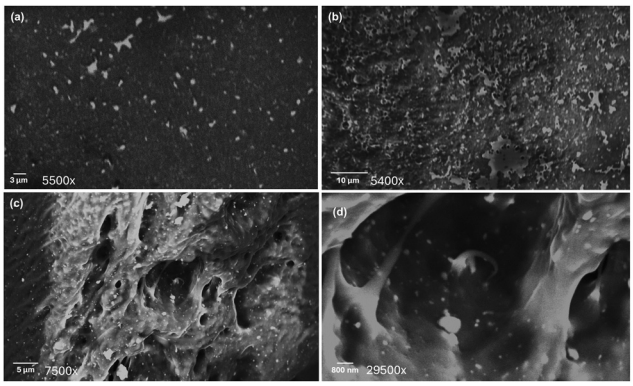

Fig. 7 E-SEM images of 10-LNC (a), 10-L + A (b), and 5-LNC (c) and (d).

matrix, oftentimes many micrometers in diameter (Fig. 7b), further indicating that the lignin is indeed acting as a container for the APP. There was a reduction in the dispersion efficiency of the LNCs between sample 10-LNC (Fig. 7a) and 5-LNC (Fig. 7c), as the 5-LNC sample manages to retain spherical LNCs in contrast to the clear aggregation in some area of the 10-LNC sample. Fig. 7d provides an overview of the size distribution of the LNCs, as particles range in size from 100 nm to 1 µm as discussed in the DLS analysis section (Fig. 4b). All SEM images can be found in the supplementary information section (Fig. S2–S6).

3.2. Material characterization

3.2.1. Mechanical properties. The incorporation of LNCs to natural rubber generally improved all mechanical properties (Fig. 8); the composites were stronger, stiffer, more ductile, and tougher than sample N which has been seen previously with other nano-lignin + natural rubber composites.[32] When comparing samples N and 2.5-LNC, the minor addition of LNCs cause spikes to the modulus and hardness, but all other properties remained the same as that of sample N. Sample 5-LNC is where increases were seen overall, with a maximum increase at 10-LNC with properties decreasing significantly with sample 15-LNC indicating an optimal loading at 10 wt% in terms of mechanical properties. In terms of percent change, sample 10-LNC saw a 35% increase to the ultimate tensile strength, a 61% increase to the modulus, a 51% increase to the elongation at break, a 127% increase to the toughness, and a 65% increase to the hardness compared to sample N. Sample 10-L + A did outperform sample 10-LNC in terms of tensile strength and tensile modulus, but did have a lower elongation at break. This shows that the increases to tensile strength and modulus are due to increasing filler content. But the form of said additive matters, as the nanomaterial tended to disrupt the rubber matrix less, leading to a larger elongation at break compared to sample LNC-L + A.

3.2.2. Thermogravimetric analysis (TGA). From the TGA analysis, all rubber composites displayed one major decomposition stage with a minor onset stage (Fig. 9a). The minor mass loss for NR compounds at the onset (150–300 °C) is typically associated with the volatilization of oils,[33] and was attributed to the breakdown of short-chain polymers that generate the oils. The major decomposition (300–450 °C) is associated with the fragmentation of natural rubber, which generates various hydrocarbon gases.[34] With increasing FR content, the major decomposition yielded lower DTG peaks (Fig. 9a) due to the increased charring.

Generally, as the concentration of the LNCs increased, so did the char yield. This increase is largely due to lignin's charring characteristics,[21] where it preferentially decomposes its aliphatic units through dehydration over its aromatic ones, forming a complex polyaromatic char.[35,36] APP also catalyzes the dehydration of materials to promote char formation, forming more stable and dense chars.[16] The 2.5-LNC sample had a practically identical char value to sample N, with a large jump of 2.43% char when compared to sample 5-LNC. Another major increase of 4.56% was seen between sample 10-LNC and 15-LNC, which are both of similar magnitude when considering the relative change in LNC content. Interestingly, the 10 wt% samples all yielded differing char amounts, with the foamed sample (10-LNC (f)) yielding the largest amount (at 6.73%), 1.72% more than the lowest char yield at that same concentration (10-LNC) (Fig. 10). The porous nature of the foam slows the diffusion of gases generated during devolatilization, promoting additional charring rather than devolatilization during TGA, so increased porosity can increase the char yield in some cases.[37]

The thermal decomposition under air (Fig. 11) was very similar to that observed under nitrogen, except for an additional minor decomposition step between 450–550 °C,

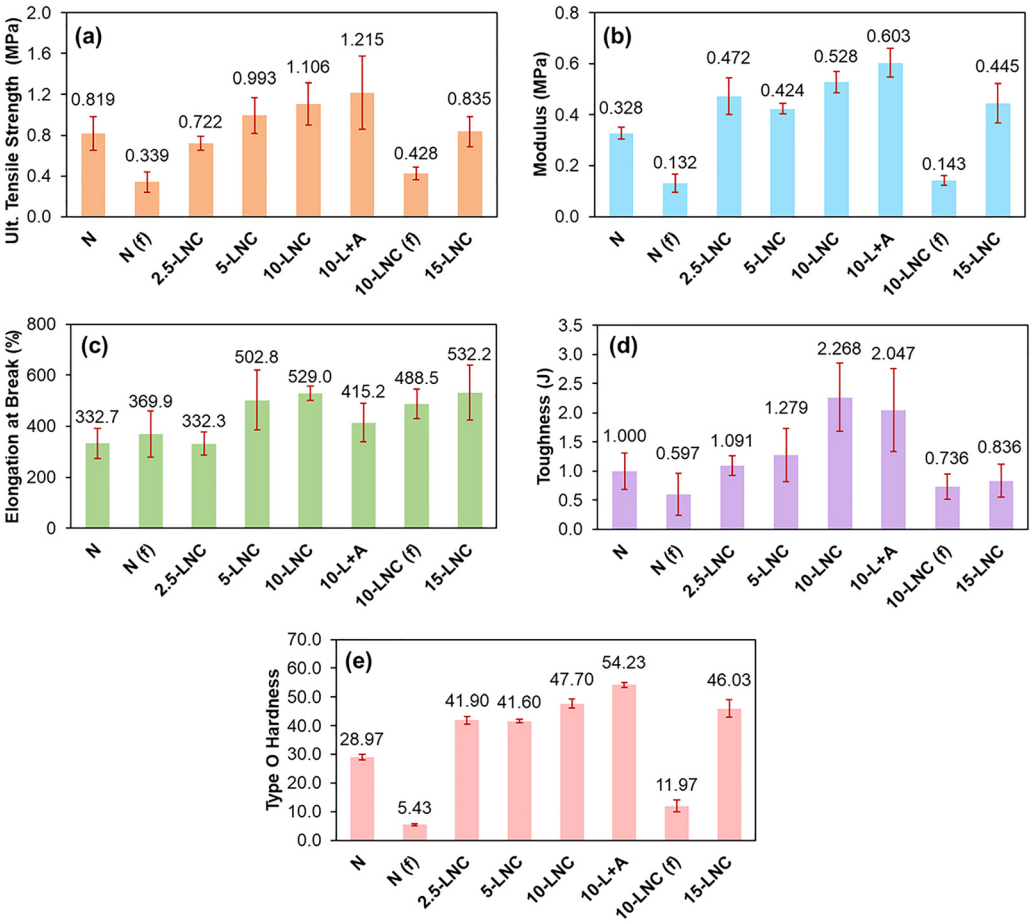

Fig. 8 Mechanical data for ultimate tensile strength (a), Young's modulus (b), elongation at break (c), toughness (d), and type O hardness (e). Error bars indicate ± one standard deviation.

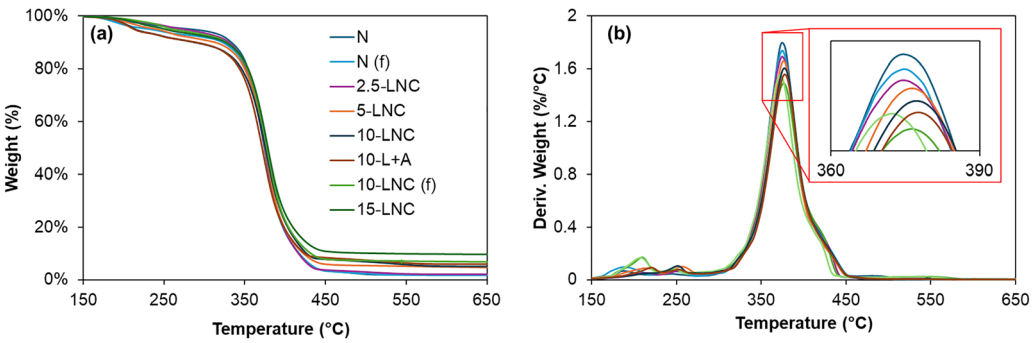

Fig. 9 TGA (a) and DTG (b) curves – under nitrogen.

attributed to the combustion of organic materials.[33] Additionally, all samples tended to decompose slightly faster under air, for example, the peak rate for 5-LNC was 1.66%/°C under nitrogen compared to 1.74%/°C under air.

3.2.3. Flammability testing

3.2.3.1. Combustion indices. Utilizing the TGA data under air, the combustion indices for all samples were calculated using eqn (1)–(4) (Fig. 12a). To better illustrate the trends, the percent "improvement" for each sample was calculated with respect to sample N (Fig. 12b), where a decrease in any combustion index represents an improvement in flame retardancy. Across all samples, index *C* showed the least change, frequently showing a change of less than 10%, indicating that any rise/reduction in the max heating rate was offset by changes in the ignition temperature. As shown in Fig. 11a, increasing the FR content tended to reduce the max heat rate, but also

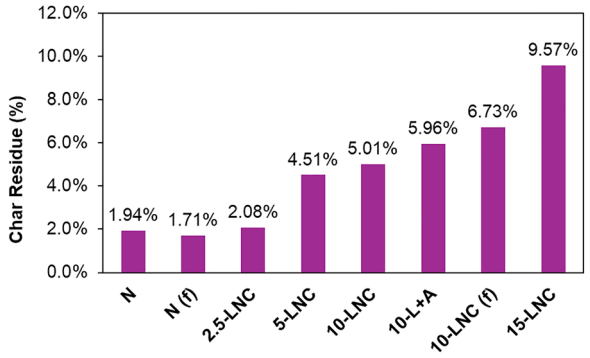

Fig. 10 Char values following inert TGA.

lowered the ignition temperature. The most notable improvements were observed in index S and D_b, which increased in a somewhat linear fashion with higher LNC content, plateauing at roughly 35% improvements between samples 10-LNC and 15-LNC. These improvements indicated that the LNC are generating dense chars during combustion that limit the rate of mass loss while maintaining the thermal stability of the material. In contrast, sample 10-L + A showed a pronounced decline in performance – index C and D_i worsening by 21% and 49%, respectively. While many other samples saw slight reductions, the decrease in improvement to D_i for 10-L + A indicate a worse thermal stability as it is affected by the max rate, ignition time, and time to reach the max rate. The 10-L + A sample also did not have the improvements to D_b as was seen with the other samples, but still retained some improvement to S. This indicates the inability of sample 10-L + A to retain its shape during combustion and would likely lose its mechanical properties quicker than an LNC sample.

Foaming also had a notable effect. The foamed sample N (sample N (f)) showed improvements in both S and D_b, likely because its pore structure promoted the formation of a porous char, which can act as a greater barrier to heat transfer than a solid char under non-flaming conditions. Meanwhile, sample 10-LNC (f) had very similar performance to that of 10-LNC, albeit a much better D_i.

3.2.3.2. SDT Analysis. The combustion indices are based on mass loss curves, but a more complete analysis requires investigating the actual heat released by the samples during combustion events.[38] Fig. 13 presents the HRR for select samples, all of which exhibit two major peaks, with the combustion calorimetry parameters shown in Table 2. The first peak (~400 °C) aligns with the major TGA peak (Fig. 11a) and represents the generation of hydrocarbon gases from sample N, while the second peak (~500 °C) corresponds to the combustion peak. As shown below, the primary heat release occurs during combustion, whereas the combustion indices emphasized the first peak. Consistent with the combustion indices, sample N displayed the poorest fire performance, generating the highest heat release, though sample N (f)

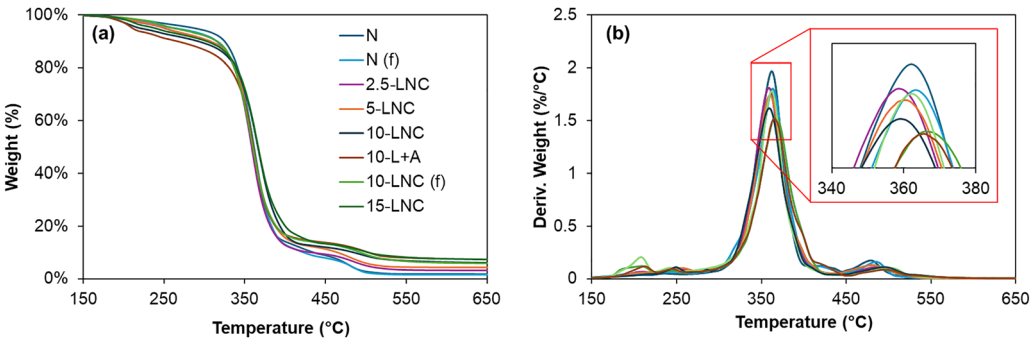

Fig. 11 TGA (a) and DTG (b) curves – under air.

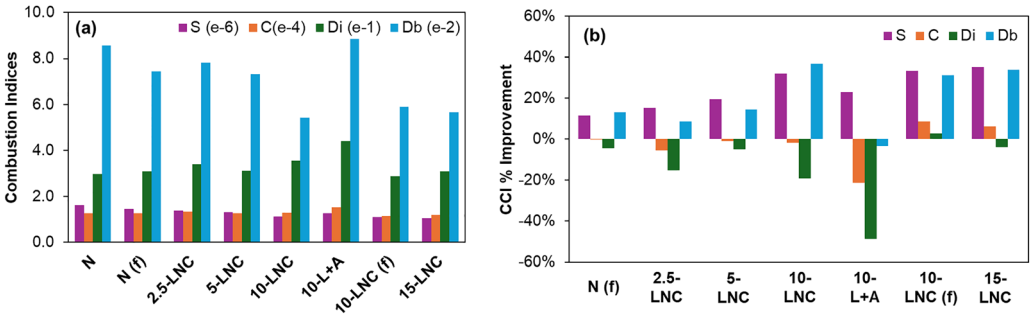

Fig. 12 Combustion indices, S (min^{-2} K^{-3}), C (min^{-1} K^{-2}), D_i (min^{-3}), & D_b (min^{-4}), (a) and percentage improvement for samples relative to the values of sample N (b).

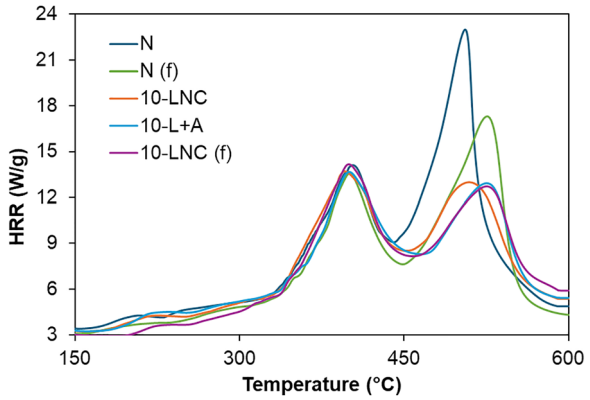

Fig. 13 HRR curves for select samples measured *via* SDT.

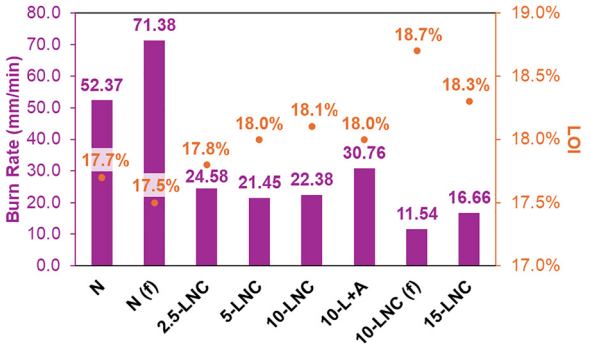

Fig. 14 Linear burn (purple) and LOI data (orange).

exhibited noticeable improvement. This was attributed to the cell structure of the rubber foam acting as a thermal insulator preventing internal heat generated *via* combustion from escaping the sample. All other samples which contained 10 wt% FR showed very similar results to one another, all lowering the combustion pHRR by approximately 40%. Between them, the 10-L + A sample outperformed the 10-LNC sample slightly, with lower parameters across the board. The best performance was observed for the 10-LNC (f) sample, which achieved the lowest FGC (80.15), representing a 13.7% reduction compared to sample N. Overall, these results indicate that the sample form has some impact on the heat release during the combustion, whereas filler concentration exerts a much stronger effect.

3.2.3.3. Linear Burn & LOI. The linear burn rate and LOI results are presented in Fig. 14, showing a strong inverse relationship between the two tests. As the linear burn rate decreases, the LOI increases – both indicating improved flame retardancy. However, all samples exhibited an LOI below 21%, suggesting that they will readily burn under atmospheric conditions. This indicates the LNCs lack the strength to enhance natural rubber to be self-extinguishing.

All LNC-loaded samples performed very similarly with an approximate 58% decrease to linear burn, with the 15-LNC sample being closer to a 67% decrease. Unlike the earlier non-flaming assessments, sample N (f) performed worse here, as its porous structure facilitated flame propagation. From this, we could expect that sample 10-LNC (f) would perform worse in comparison to sample 10-LNC, but this was not the case. In fact, the 10-LNC (f) sample showed the best performance, with a 78% reduction in burn rate compared to sample N (and an 84% reduction compared to sample N (f)), suggesting a possible synergistic effect between foamed structures and LNCs, likely strengthening the intumescent effect of the APP.[6] In certain polymer systems, additional charring and foaming agents are added in conjunction with APP, even though APP itself is considered intumescent.[39] This highlights the importance of a porous char and would indicate additional blowing agents required for non-foamed samples to achieve satisfactory intumescency.

Table 2 Heat release data for select samples obtained *via* SDT

	pHRR (W g^{-1})	mHRR (W g^{-1})	T_{pHRR} (°C)	THR (kJ g^{-1})	$T_{5\%}$ (°C)	$T_{95\%}$ (°C)	FGC (J g^{-1} K^{-1})
N	22.99	9.16	505.58	10.89	199.36	557.35	92.83
N (f)	17.31	7.93	525.85	10.46	202.16	598.43	85.36
10-LNC	13.72	8.20	395.62	9.90	198.70	562.48	84.13
10-L+A	13.66	8.07	399.99	9.76	198.27	562.80	83.05
10-LNC (f)	14.17	7.96	399.67	9.57	202.59	566.45	80.15

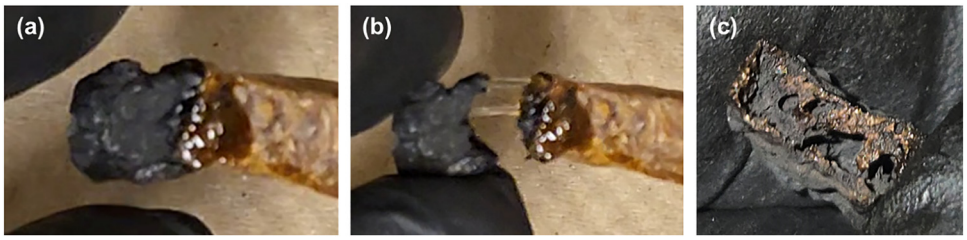

Fig. 15 Images of sample 5-LNC after LOI showcasing the char formed during burning (a, b), and the char's porous structure (c).

Table 3 UL-94 horizontal burn (HB) test ratings

	Rating
N	Failed
N (f)	Failed
2.5-LNC	HB
5-LNC	HB
10-LNC	HB
10-L + A	HB
10-LNC (f)	HB
15-LNC	HB

As LNC concentration increased, more pronounced char formation was observed, unlike sample N, which primarily decomposed into a greasy, short-chain polymer residue. This greasy residue can be seen in Fig. 15a and b, just below the site of burning. Fig. 15c showcases the char formed from sample 10-LNC after an LOI test. The char structure laid on top of the site of burning and formed a somewhat porous structure (Table 3).

The improvements in LOI and UL-94 HB performance correlate strongly with TGA-derived reductions in mass-loss rate and increased char yield, confirming that the LNC-mediated intumescent char acts as an effective thermal barrier. Samples with inferior char stability (*e.g.*, bulk lignin/APP addition) displayed poorer combustion indices and less favorable UL-94 outcomes despite similar filler loadings.

Conclusions

Kraft lignin–based nanocontainers (LNCs) were successfully developed to deliver a hydrophilic flame retardant within a hydrophobic natural rubber (NR) matrix, enabling uniform nanoscale dispersion and suppressing additive aggregation during latex processing. This nanocontainer-mediated approach allowed effective flame retardancy to be achieved at relatively low loadings while preserving processability. At an optimal loading of 10 wt% LNC, the NR composites exhibited a 35% improvement in combustion indices, a 43% reduction in peak heat release rate, and a 57% decrease in linear burn rate relative to neat NR. These improvements were accompanied by a 127% increase in toughness and concurrent gains in strength, stiffness, and elongation at break, demonstrating that flame resistance was enhanced without sacrificing mechanical performance. In contrast, bulk addition of lignin and ammonium polyphosphate resulted in inferior combustion behavior, highlighting the advantages of nano-encapsulation. Foamed NR/LNC composites showed further improvements in flame performance, including higher limiting oxygen index values and substantially reduced linear burn rates compared to solid counterparts, indicating a synergistic interaction between the intumescent nanocontainers and the porous foam structure. Although the limiting oxygen index remained below the threshold for self-extinguishing behavior, the reductions in heat release and burn rate represent meaningful gains in fire safety. Overall, lignin nanocontainers offer a scalable, bio-based strategy for balancing flame retardancy and mechanical performance in sustainable rubber composites.

Conflicts of interest

There are no conflicts to declare.

Data availability

Data will be made available on request.

Supplementary information (SI) is available. See DOI: https://doi.org/10.1039/d5ma01531f.

Acknowledgements

We acknowledge the financial support of the Natural Sciences and Engineering Research Council of Canada (NSERC), and the Canada Foundation for Innovation (CFI). This research was undertaken, in part, thanks to funding from the Canada Research Chairs Program.

References

1 J. G. Rosenboom, R. Langer and G. Traverso, *Nat. Rev. Mater.*, 2022, **7**, 117–137.
2 Y. Ikeda, T. Phakkeeree, P. Junkong, H. Yokohama, P. Phinyocheep, R. Kitano and A. Kato, *RSC Adv.*, 2017, **7**, 5222–5231.
3 S. Araby, B. Philips, Q. Meng, J. Ma, T. Laoui and C. H. Wang, *Composites, Part B*, 2021, **212**, 108675.
4 S. Junian, M. Z. H. Makmud and J. Sahari, *J. Adv. Res. Mater. Sci.*, 2019, **1**, 1–12.
5 L. Wan, C. Deng, Z. Y. Zhao, H. Chen and Y. Z. Wang, *Polymers*, 2020, **12**, 429.
6 S. Peil, R. Mouhoubi, R. Streekstra, H. Ridard, L. Veith, W. Ali, T. Mayer-Gall, J. Duvigneau and F. R. Wurm, *ACS Appl. Polym. Mater.*, 2024, **6**, 6096–6107.
7 R. Silva, A. Barros-Timmons and P. Quinteiro, *J. Cleaner Prod.*, 2023, **430**, 139697.
8 W. He, P. Song, B. Yu, Z. Fang and H. Wang, *Prog. Mater. Sci.*, 2020, **114**, 100687.
9 ASTM, ASTM Stand., 2011, pp. 1–14.
10 X. Zhao, Y. Liu, B. Sun, Z. Liu, Z. B. Shao, X. Liu, H. Zhang, Z. Sun and W. Hu, *J. Appl. Polym. Sci.*, 2023, **140**, 1–10.
11 R. Sauerwein, *Non-Halogenated Flame Retardant Handbook*, Wiley, 2nd edn, 2021, pp. 101–168.
12 A. B. Morgan and J. W. Gilman, *Fire Mater.*, 2013, DOI: 10.1002/fam.2128.
13 S. Shaw, *Rev. Environ. Health*, 2010, **25**(4), 261–305.
14 M. M. Velencoso, A. Battig, J. C. Markwart, B. Schartel and F. R. Wurm, *Angew. Chem., Int. Ed.*, 2018, **57**, 10450–10467.
15 H. Nabipour and Y. Hu, *Bio-based Flame-Retardant Technol. Polym. Mater.*, 2022, 1–27.
16 X. C. Jiang, P. Li, Y. Liu and J. S. Wang, *Cellulose*, 2023, **30**, 1321–1334.

17 H. Lavrenyuk, B. Mykhalichko, P. Garanyuk and O. Mykhalichko, *Fire Mater.*, 2020, **44**, 825–834.
18 O. E. Akindele, E. G. R. dos Anjos, A. B. Mapossa and U. Sundararaj, *Recycling*, 2025, **10**, 45.
19 M. M. Y. M. Zaghloul, *J. Appl. Polym. Sci.*, 2018, **135**, 46770.
20 P. Alikiotis and T. H. Mekonnen, *Int. J. Biol. Macromol.*, 2025, **321**, 146527.
21 D. Jubinville, R. Sen, P. Alikiotis and T. H. Mekonnen, *J. Vinyl Addit. Technol.*, 2025, **31**(5), 1138–1150.
22 S. B. Patrícia, X. Erdocia, D. A. Gatto and J. Labidi, *Ind. Crops Prod.*, 2014, **55**, 149–154.
23 R.-C. Sun, *ChemSusChem*, 2020, **13**, 4385–4393.
24 X. C. Jiang, P. Li, Y. Liu, Y. W. Yan and P. Zhu, *Ind. Crops Prod.*, 2023, **197**, 116611.
25 W. Lu, Q. Li, Y. Zhang, H. Yu, S. Hirose, H. Hatakeyama, Y. Matsumoto and Z. Jin, *J. Wood Sci.*, 2018, **64**, 287–293.
26 Q. Yang, T. Wang, J. Wang, Z. Sui, L. Wang, Y. Zhang and W.-P. Pan, *Thermochim. Acta*, 2021, **702**, 178979.
27 J. Huang, J. Liu, J. Chen, W. Xie, J. Kuo, X. Lu, K. Chang, S. Wen, G. Sun, H. Cai, M. Buyukada and F. Evrendilek, *Bioresour. Technol.*, 2018, **266**, 389–397.
28 R. E. Lyon, N. Safronava, S. Crowley and R. N. Walters, *Polym. Degrad. Stab.*, 2021, **186**, 109478.
29 E. Burzo, *Spectroscopy*, 2023, **38**, 14–16.
30 C. A. Cateto, M. F. Barreiro and A. E. Rodrigues, *Ind. Crops Prod.*, 2008, **27**, 168–174.
31 A. Eraghi Kazzaz and P. Fatehi, *Ind. Crops Prod.*, 2020, **154**, 112732.
32 C. Jiang, H. He, H. Jiang, L. Ma and D. M. Jia, *eXPRESS Polym. Lett.*, 2013, **7**, 480–493.
33 M. J. Fernández-Berridi, N. González, A. Mugica and C. Bernicot, *Thermochim. Acta*, 2006, **444**, 65–70.
34 T. Kan, V. Strezov and T. Evans, *Fuel*, 2017, **191**, 403–410.
35 J. Ruwoldt, F. H. Blindheim and G. Chinga-Carrasco, *RSC Adv.*, 2023, **13**, 12529–12553.
36 R. K. Sharma, J. B. Wooten, V. L. Baliga, X. Lin, W. G. Chan and M. R. Hajaligol, *Fuel*, 2004, **83**, 1469–1482.
37 M. Thirumal, D. Khastgir, N. K. Singha, B. S. Manjunath and Y. P. Naik, *J. Appl. Polym. Sci.*, 2008, **110**, 2586–2594.
38 A. B. Morgan, *Polym. Rev.*, 2019, **59**, 25–54.
39 A. B. Mapossa, N. Mohammad Mehdipour and U. Sundararaj, *J. Vinyl Addit. Technol.*, 2025, **31**, 146–181.